Nano Energy 92 (2022) 106738

Contents lists available at ScienceDirect

Nano Energy

journal homepage: www.elsevier.com/locate/nanoen

Ion regulation in double-network hydrogel module with ultrahigh thermopower for low-grade heat harvesting

Chang Liu [a,b,1], Qikai Li [a,c,1], Sijia Wang [a], Weishu Liu [c], Nicholas X. Fang [b,*], Shien-Ping Feng [a,*]

[a] Department of Mechanical Engineering, The University of Hong Kong, Pokfulam Road, 999077, Hong Kong, China
[b] Department of Mechanical Engineering, Massachusetts Institute of Technology, Cambridge, MA 02139, USA
[c] Department of Materials Science and Engineering, Southern University of Science and Technology, Shenzhen, Guangdong 518055, China

ARTICLE INFO

Keywords:
ionic thermoelectric systems
thermopower
ion transport
double-network hydrogel
low-grade heat harvesting
2D-diffusion-ordered spectroscopy

ABSTRACT

Harvesting low-grade heat as source of electrical power has emerged as a research frontier for self-powered wearable devices, as a promising route to overcome challenges associated with limited access to grid power. However, such promise is compromised by current attainable thermopowers and constraints of rigid or complicated thermoelectric systems. We report an ultrahigh thermopower of 19.32 mV K^{-1} on a stretchable thermoelectric module by the assembly of porous electrodes and hybrid hydrogel, containing 1-ethyl-3-methylimidazolium and tetrafluoroborate ions and polyethylene glycol. The anions act as charge carrier; for the first time, distinct ion mobilities are directly measured by 2D-diffusion-ordered nuclear magnetic resonance spectroscopy. By regulating ion transport via the synergy of selective ion-localization and thermo-osmotic mechanism, such design provides an effective strategy to increase thermopower, and our device is endowed with high output power density, tailorable architecture, and excellent stretchability, which is showcased in a thermoelectric wristband for body heat recovery.

1. Introduction

From primary power generation to data centers and even human bodies, extracting energy from ubiquitous source of heat with temperature less than 100 °C has been a fast-moving research frontier due to the abundance and inexpensiveness of low-grade heat [1]. Especially, the emerging demands for ever-expanding array of wearable electronics for health monitoring call for off-grid environmental energy capture, and there is a resurging interest of body heat because of its accessibility, sustainability, and environmental benign nature. In addition to easy adoption to wearable power supply, new materials and modules of mechanical flexibility and tailorable architecture are desirable [2–4].

To convert low-grade heat into electricity, two types of mechanisms are often found in common modules: the Seebeck effect of thermoelectric semiconductors (TEs) and thermogalvanic effect of thermoelectrochemical cells (TECs). The former is based on the temperature-induced transport of electrons or holes, which carry both charge and heat. The Seebeck coefficient (*Se*) is depicted as the entropy transported per charge transported. The strong dependence of *Se* on carrier concentration in such semiconductors is manifestation of an effective mass of the carrier near the Fermi surface [5,6]. Even the most promising TEs are limited by *Se* of sub-mV K^{-1} [7–9]. As a consequence, to drive common electronic sensors at a few volts, it requires assembling thousands of n-type and p-type thermopiles.

At first glance, a remarkable advantage of voltage output can be brought by aqueous TECs as they rely on redox reactions. The entropy change associated with specific redox couple in TECs often sets the temperature coefficient (α) to a few mV K^{-1}, which still barely affords sufficient voltage with single layer of few stacks [2]. Meanwhile, the complexity and reliability issues associated with the aqueous system may arise since thermogalvanic cell (TGC) or thermally regenerative electrochemical cycle (TREC) [10,11], require special cell configurations or undergo four-stage settings, respectively [2,3].

Leveraging the richness of ions as charge carriers, ionic thermoelectric systems (i-TEs) provide alternative route to improve thermopower (S_i) via the Soret effect [12–15]. Such optimism is supported by recent discovery of an impressive S_i of 24 mV K^{-1} in an aqueous solution with a cellulosic membrane, while sodium cation (Na^+) is mobile while hydroxide anion (OH^-) is localized [12]. Yet, the encapsulation of the aqueous system limits the compatibility to wearable power supply [3].

* Corresponding authors.
E-mail addresses: nicfang@mit.edu (N.X. Fang), hpfeng@hku.hk (S.-P. Feng).
[1] These authors contribute equally to this work.

https://doi.org/10.1016/j.nanoen.2021.106738
Received 25 July 2021; Received in revised form 20 October 2021; Accepted 9 November 2021
Available online 14 November 2021

Here we report a quasi-solid-state i-TE using a hydrogel comprising 1-ethyl-3-methylimidazolium tetrafluoroborate ($EmimBF_4$) ionic liquid (IL) and polyethylene glycol (PEG) polymer, which not only imbibes great water content and swells dissolving salts, but also provides substantial polymer chains and functional groups for regulation of ion transport [16]. The anions perform as charge carrier and for the first-time distinct ion mobilities are directly observed by 2D-diffusion-ordered spectroscopy (DOSY) nuclear magnetic resonance (NMR). This newly designed i-TE exhibits giant S_i and high output power density. Additionally, our i-TE can be made in a variety of sizes and shapes, and of which the excellent stretchability is showcased in a thermoelectric wristband (Fig. 1A), paving the way for new forms of low-grade heat harvesters for wearable power supply.

2. Results and discussion

2.1. Thermoelectric performance

To elaborate the regulation of ion transport in the hydrogel, we conducted experiments on a model system of poly(acrylamide) and alginate (Pam-alginate) double-network hydrogel containing $EmimBF_4$ IL and PEG (Fig. 1B), sandwiched by nanoporous carbon paper (CP) electrodes, which are permeable to water and vapor (Fig. S1), connecting with titanium (Ti) leads. The entire system is sealed by a polyolefin wrap for preventing water loss. We named it as Pam-alginate/$EmimBF_4$/PEG and Fig. 1C schematically illustrates our proposed mechanism. In a binary ionic system, the thermovoltage ($V_{thermal}$) is produced by asymmetric ion accumulation across hot and cold electrodes, which is proportional to the difference in mobility between cation and anion [17]. In the absence of temperature difference, the high water content in the Pam-alginate hydrogel benefits to a complete dissociation of $Emim^+$ and BF_4^-. When a temperature gradient is built across two nanoporous CP electrodes, local vapor pressure is developed proportional to the pore scale, magnifying the pump force as a function of surface tension driven by local temperature. The change in vapor pressure promotes a higher water evaporation rate towards the hot end, driving a net ion flux with water convection [18]. Indeed, we observed the condensation of water droplets at the cold end, similar to the circulation of water in heat pipes. Here, BF_4^- anion is electrostatically repelled by the hydrogel matrix containing carboxylate groups, becoming more mobile than $Emim^+$ cation, whereas $Emim^+$ experiences electrostatic attraction from the hydrogel matrix and meanwhile PEG chains provide additional hydrogen bonding to selectively localize $Emim^+$ [19,20]. As a result, the accumulation of BF_4^- within the hydrogel is highly dependent on local temperature, while $Emim^+$ are condensed on the PEG chains and the hydrogel matrix. In our study, an excessive charge at the hot electrode due to accumulation of BF_4^- is responsible for the observed voltage $V_{thermal}$.

Analogous to *Se* in TEs, the thermopower is calculated as $S_i = -\frac{V_{thermal}}{\Delta T}$ for i-TEs at a given temperature difference (ΔT) [10]. Fig. 2A shows the $V_{thermal}$ versus ΔT plot of a Pam-alginate/$EmimBF_4$/PEG, which was made by an optimized two-step electrolyte infiltration process in 1.3 M $EmimBF_4$ for 16 h and 0.05 g ml^{-1} PEG for 1 h. (Unless otherwise stated, the Pam-alginate/$EmimBF_4$/PEG were prepared as described above.) We also conducted a series of experiments by varying the $EmimBF_4$ and PEG compositions from which the Pam-alginate/$EmimBF_4$/PEG was prepared (see Supplementary Note 1, Figs. S2–S6). The $V_{thermal}$ gradually changes from 2.9 mV to −34.3 mV when a ΔT of 2.3 °C is built between two CP electrodes and the $V_{thermal}$ further changes to −72.1 mV at a ΔT of 3.9 °C and so forth. The S_i of this Pam-alginate/$EmimBF_4$/PEG champion sample is calculated to be 19.32 mV K^{-1} (Fig. 2B), ranks among the highest reported thermopowers (Fig. 2C) [2,4,12,13,21–29]. Unlike the situation in TECs or i-TEs with solid electrodes (e.g., gold films), the water permeability of the porous electrode is dependent on the osmotic state of hydrogel at given temperatures in our system (see Supplementary Note 2). Herein, Pam-alginate/$EmimBF_4$/PEG is paired up with nanoporous CP electrodes, where the ion transport is governed by temperature-induced vapor pressure difference and selective cation-localization within the hydrogel collectively. In comparison, we present the results in Fig. S7 when graphite sheet and Au foil are used as electrodes impermeable to water. In these cases, the water evaporation through the electrode at the hot end was prohibited,

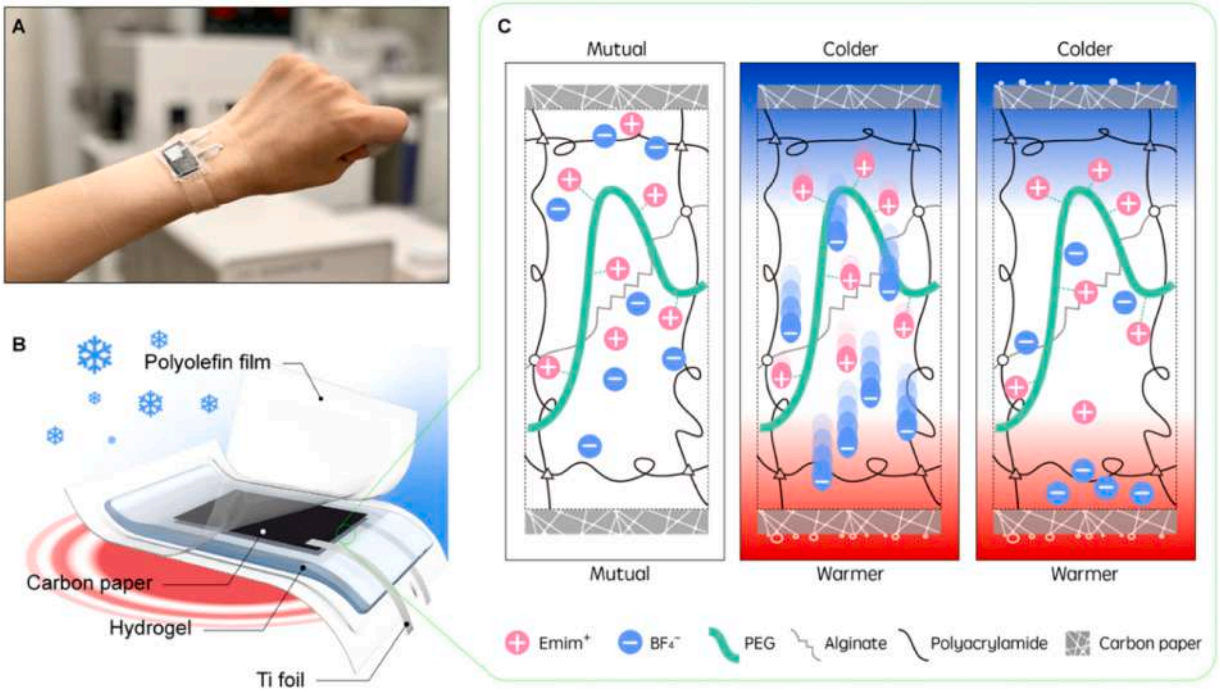

Fig. 1. Pam-alginate/$EmimBF_4$/PEG. (A) Digital image of a thermoelectric wristband made of Pam-alginate/$EmimBF_4$/PEG. (B) System of Pam-alginate/$EmimBF_4$/PEG consisting of Pam-alginate hydrogel electrolyte including $EmimBF_4$ IL and PEG, nanoporous CP electrodes, Ti conductors and polyolefin wrap. (C) Schematic illustration of generating thermovoltage in Pam-alginate/$EmimBF_4$/PEG.

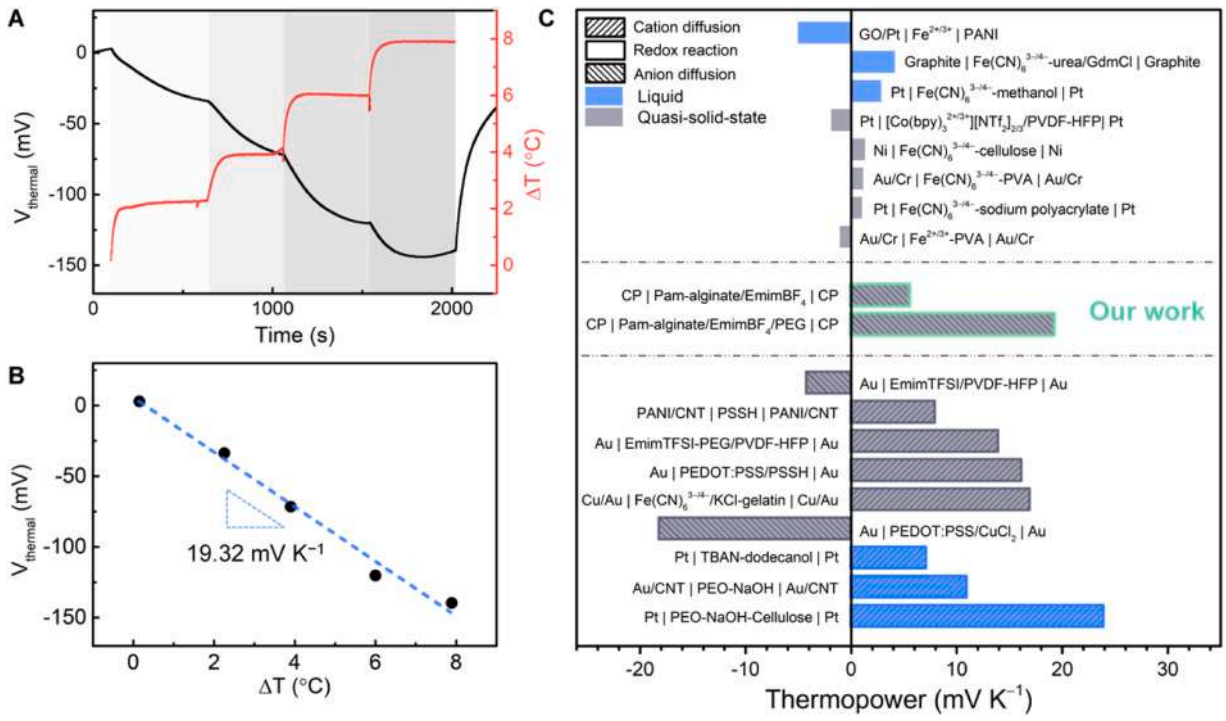

Fig. 2. Thermopower characterization. (A) Thermovoltage versus temperature gradient plot. (B) Thermopower of Pam-alginate/$EmimBF_4$/PEG. (C) Comparison of thermopower for Pam-alginate/$EmimBF_4$/PEG with some of the best reported TECs and i-TEs (see Appendix). The thermoelectric systems inclusive of electrolytes and electrodes are presented.

so that the ion transport was dominated by the thermo-diffusion of BF_4^- towards the cold electrode, leading to a negative thermopower ranging from -1.09 mV K^{-1} to -0.81 mV K^{-1}. Especially, a positive thermopower of 0.56 mV K^{-1} was obtained when the Au foil was replaced by Au mesh with pore size of 150 μm (Fig. S7). These findings highlight the key effect of transpiration-driven ion transport to the augmented thermopower in our system.

2.2. Regulation of ion transport

Pam-alginate hybrid hydrogel is chosen as the matrix for IL in this work because first of high water content of ~86%, which allows the sufficient dissociation of two ionic species (i.e., $Emim^+$ and BF_4^-) [30]. Our strategy is inspired by the unique hydrogel under sharks' skin that can translate the abrupt thermal stimulus into an electric stimulus based on small shifts in local ionic concentration [31,32]. The second prerequisite is that the Pam-alginate double-network hydrogel possesses substantial carboxyl functional groups on alginate chains which exert electrostatic attraction to $Emim^+$ but repulsion to BF_4^- (as illustrated in Fig. 3A). Third, the PEG long chains are physically entangled with the hydrogel matrix, meanwhile, selectively impede the ion transport of $Emim^+$ through hydrogen bonding [19,20], which help to enlarge the disparity in the mobility between $Emim^+$ and BF_4^-.

To test our hypothesis on the electrostatic modulation of the hydrogel matrix for regulating ion transport, the control experiments were conducted on pure Pam/$EmimBF_4$, pristine Pam-alginate/EmimBF4 and pure alginate/$EmimBF_4$, exhibiting the S_i of 2.13 mV K^{-1}, 5.61 mV K^{-1} and 20.7 μV K^{-1}, respectively (Fig. S8). In a pure Pam/$EmimBF_4$ with a water content of ~90%, the anions are easier to move than the cations since the volume of BF_4^--H_2O complex is smaller than that of $Emim^+$-H_2O complex [30]. In the pristine Pam-alginate/$EmimBF_4$, a higher S_i is observed because the electrostatic attraction of carboxyl group on alginate impedes the ion transport of $Emim^+$ whereas that of BF_4^- through the hydrogel is facilitated by the electrostatic repulsion of carboxyl group, inducing an enlarged disparity in mobility between $Emim^+$ and BF_4^-. In the pure alginate/$EmimBF_4$ with the water content less than 10%, $EmimBF_4$ is difficult to dissociate and mainly forms ion pair-water complexes [30], thereby its S_i is very small with the lack of dissociated ions. Furthermore, $LiBF_4$ was used to replace $EmimBF_4$ in the pristine Pam-alginate hydrogel with S_i being reduced to 1.85 mV K^{-1} (Fig. S9). Likewise, the ion transport of Li^+ is hindered by the electrostatic attraction of carboxyl group in the hydrogel, yet the disparity of mobility between Li^+ and BF_4^- anions is compromised since the hydrated Li^+ is smaller in volume compared with BF_4^--H_2O complex, which overall results in a smaller S_i.

Apart from the aforementioned effects arising from the nature of $Emim^+$ and BF_4^-, the disparity in mobility is significantly enlarged by introducing PEG long chains. Here, the diffusion coefficient of $Emim^+$ and BF_4^- was systematically investigated by using DOSY ^1H and ^{19}F NMR. Fig. 3B and Fig. 3C show 1D ^1H NMR spectrum of $Emim^+$ and ^{19}F NMR spectrum of BF_4^- with the peak assignments, respectively, where an additional peak of chemical shift at 3.79 ppm is assigned to PEG [33,34]. We applied the pulsed gradient spin echo (PGSE) technique in 2D DOSY NMR for both liquid and hydrogel samples (see Methods and Supplementary Note 3). Fig. S10 and Fig. S11 show ^1H NMR and ^{19}F NMR spectra of four samples including pure $EmimBF_4$ aqueous solution and $EmimBF_4$ aqueous solutions with three different concentrations of PEG. The signal intensity (I) attenuation in terms of pulse-field gradient strength (G) was used to calculate the diffusion coefficient based on the Stejskal-Tanner equation (Fig. S12 and Fig. S13) [35]. Fig. 3D depicts that the diffusion coefficient of $Emim^+$ (D_+) decreases by ~84% from 6.44×10^{-6} cm^2 s^{-1} to 1.03×10^{-6} cm^2 s^{-1} when 10 mg ml^{-1} PEG is added, which decreases further with increasing PEG concentration. The diffusion coefficient of BF_4^- (D_-) is larger than D_+ at all PEG doses, which exhibits only a 4% reduction in the presence of 10 mg ml^{-1} PEG (from 1.22×10^{-5} cm^2 s^{-1} to 1.17×10^{-5} cm^2 s^{-1}). We also performed the first study to measure the diffusion coefficient of $Emim^+$ in the hydrogel by employing gel-phase ^1H DOSY NMR. The D_+ reveals a drastic reduction of 93% after introducing PEG into the hydrogel (Fig. S14). It is noteworthy that the decrease of D_+ with respect to

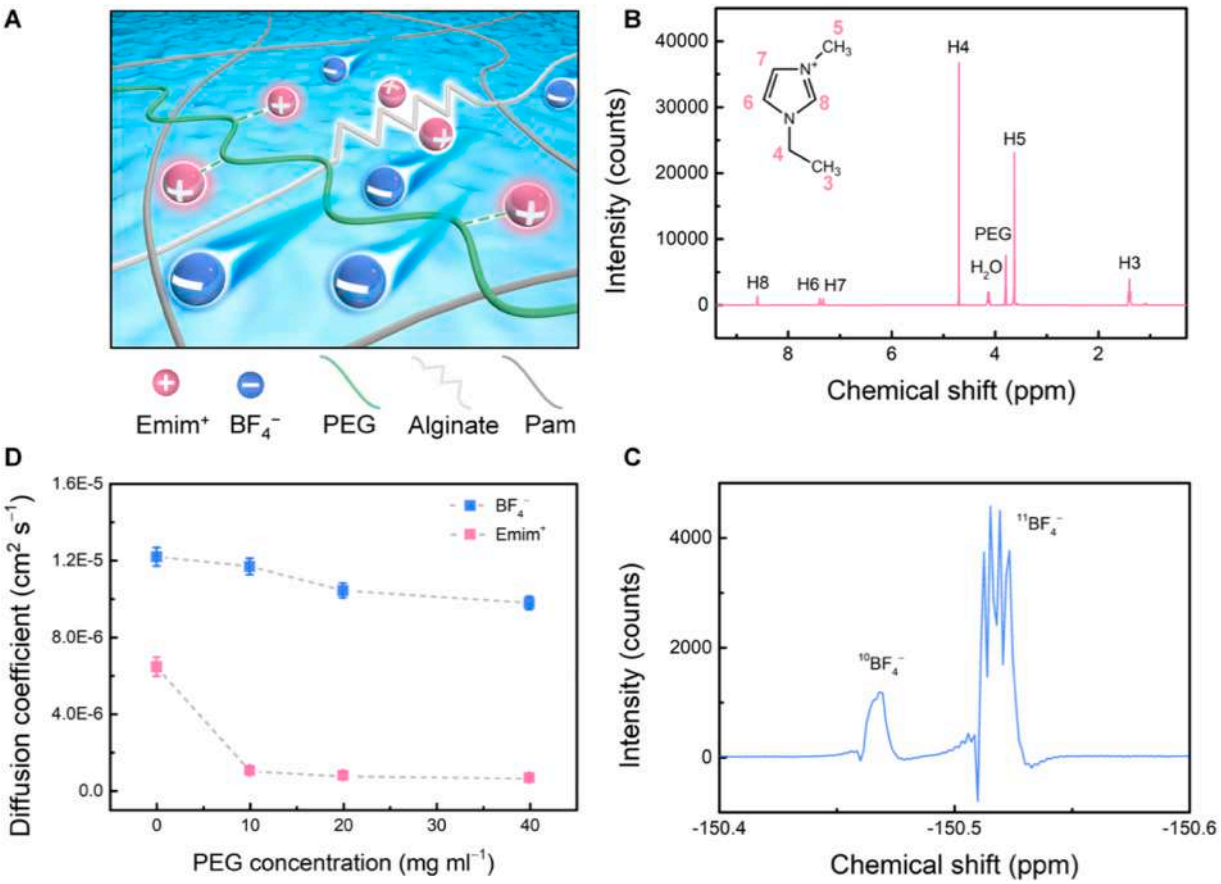

Fig. 3. Regulation of ion transport in Pam-alginate/$EmimBF_4$/PEG. (A) Schematic of selective ion-localization using Pam-alginate hybrid hydrogel mediated with PEG. The ion transport of $Emim^+$ is impeded via electrostatic attraction of alginate and hydrogen bonding with PEG chains, while the ion transport of BF_4^- is the least affected. (B) ^1H NMR spectrum of $Emim^+$ and (C) ^{19}F NMR spectrum of BF_4^- with peak assignments. (D) Diffusion coefficients of $Emim^+$ and BF_4^- as a function of PEG concentration.

adding PEG in the Pam-alginate hydrogel is more significant than that in the aqueous solution as $Emim^+$ are further localized by PEG chains entangling with the hydrogel matrix. Moreover, the in-situ heating was applied to 2D DOSY NMR for $EmimBF_4$ aqueous solution with 10 mg ml^{-1} PEG. The thermally activated BF_4^- exhibits the D_- increasing from 1.17×10^{-5} cm^2 s^{-1} at 21 °C to 1.73×10^{-5} cm^2 s^{-1} at 40 °C. In contrast, D_+ barely rises with elevating temperature, indicating that $Emim^+$ is firmly anchored by PEG (Fig. S15), conducing to the asymmetric ion transport of BF^- and $Emim^+$ in response to temperature. Here, the mobile anions predominantly behave as charge carrier in the Pam-alginate hydrogel mediated by PEG, which is distinguished from most of i-TEs relying on small cations such as Na^+ and H^+ [12,13].

On the other hand, Fig. S16A shows the Raman spectra of Pam, alginate, $EmimBF_4$, and PEG. The Raman spectrum of Pam-alginate/$EmimBF_4$/PEG was characterized by comparing the presence of the absorption bands with each pure component, which is in good agreement with the spectral overlap of all components (Fig. S16B). Exceptionally, there are two overlapping Raman bands located at 3173 cm^{-1} for pure $EmimBF_4$, which are assigned to ring HCCH symmetric stretching and ring symmetric stretching [36]. A blue shift to 3178 cm^{-1} is observed in the Raman spectrum of Pam-alginate/$EmimBF_4$/PEG, suggesting the strong confinement of $Emim^+$ on PEG via hydrogen bond [37–39].

2.3. Material characterization of Pam-alginate/$EmimBF_4$/PEG electrolyte

Electrochemical impedance spectroscopy (EIS) was used to measure the temperature dependence of ionic conductivity on the uniformly heated Pam-alginate/$EmimBF_4$/PEG sample. The ionic conductivity was calculated from 12.5 mS cm^{-1} at 10 °C to 28.0 mS cm^{-1} at 60 °C (Figs. S17A and S18), which is higher than most polymer gels and ionogels reported before (Fig. S17B) [2,26,27,40]. The high water content in Pam-alginate hydrogel not only secures the complete dissociation of $EmimBF_4$ but also facilitates the overall ion transport ascribed to a low viscosity background [16,41]. The increasing trend as a function of temperature is used to estimate the activation energy (E_a) based on the Arrhenius equation: $\sigma_T = \sigma_0 e^{-E_a/k_B T}$, where σ is the ionic conductivity, k_B is the Boltzmann constant, and σ_0 is the pre-exponential factor [12,42]. The E_a of Pam-alginate/$EmimBF_4$/PEG is 150 meV, which is higher than the 103 meV of pristine Pam-alginate/$EmimBF_4$ (Fig. S19). A higher E_a corresponds to a larger S_i.

Pam-alginate/$EmimBF_4$/PEG hydrogel exhibits a thermal conductivity (κ) of 0.53 W m^{-1} K^{-1} at 25 °C (Fig. S17C). The thermal conductivity is lower than that in aqueous systems (~0.6 W m^{-1} K^{-1}) owing to the inclusion of water and polymers in Pam-alginate/$EmimBF_4$/PEG, and of which the main polymer (i.e., Pam) has a thermal conductivity ~0.38 W m^{-1} K^{-1} [43]. Low thermal conductivity brings the merit for maintaining a steady temperature difference across two electrodes [2].

Differential scanning calorimetry (DSC) was performed in the temperature range of 20–85 °C (Fig. S17D). None of the Pam-alginate, Pam-alginate/$EmimBF_4$, Pam-alginate/$EmimBF_4$/PEG hydrogel has an endothermic peak transition during heating, which rules out the effect of phase change on S_i. Moreover, the cyclic voltammogram (CV) shows a nearly rectangular shape without redox peaks (Fig. S20), and there are negligible changes of the spectra in X-ray photoelectron spectroscopy

(XPS) for the carbon paper electrode before and after undergoing a few heating-cooling cycles (Fig. S21), evidencing the pure capacitive behavior and absence of surface redox reactions.

2.4. Power generation in Pam-alginate/EmimBF$_4$/PEG

We demonstrated the power generation of Pam-alginate/EmimBF$_4$/PEG in Fig. 4A, and of which the device was subject to thermal charging at a ΔT of 3.4 °C at open circuit condition (stage I), electrical charging using a load resistance of 1 kΩ (stage II), equilibrium with removing thermal bias and keeping the circuit open (stage III), and electrical discharging using the same load resistance of 1 kΩ (stage IV) [28]. A $V_{thermal}$ of 48.15 mV was generated at stage I, and then decreased rapidly with charges being transferred via the external circuit during stage II (Fig. 4B). Thus, an opposite voltage was created to compensate the original $V_{thermal}$. The equilibrium of charge carriers in Pam-alginate/EmimBF$_4$/PEG happened when the temperature gradient was removed. The $V_{thermal}$ was further decreased to −21.82 mV at stage III. To connect the circuit with a load resistance at stage IV, the Pam-alginate/EmimBF$_4$/PEG produced discharging current and useful work in a capacitor-like manner (Fig. 4C). Additionally, a quasicontinuous working mode was performed on a Pam-alginate/EmimBF$_4$/PEG, where the device with nearly saturated $V_{thermal}$ at a ΔT of 3.1 °C was discharged to 0 V within 8 s by connecting to an external circuit. Meanwhile, the current increased linearly from 0 to the maximum (Fig. 4D) [14]. We applied such charge-discharge cycles over 50 min and the power density of the first cycle is shown in Fig. 4E, displaying parabolic behaviors with the maximum of 0.31 μW cm^{-2}, which is at least one order higher than that of most advanced i-TEs reported recently [15,40,44,45].

2.5. Device demonstration

A 40-cycle heating-cooling test was conducted on the Pam-alginate/EmimBF$_4$/PEG device to evaluate its cyclability, which involved a thermal charging process at a ΔT of 5 °C and a cooling process at room temperature. A Pam-alginate/EmimBF$_4$/PEG sample with the initial S_i of 19.21 mV K^{-1} underwent a slight decrease and kept ~14.52 mV K^{-1} over 40 cycles (Fig. 5A). The high cyclability not only evidences the reversible temperature-induced ion transport of $Emim^+$ and BF_4^- but also indicates that the macro morphology and internal structure of the hydrogel can be well retained. The loss of surface moisture content during the first three heating-cooling cycles is suspected to be the reason for the initial decrease.

Besides the ultrahigh S_i and good cyclability, the Pam-alginate/EmimBF$_4$/PEG in the form of hydrogel possesses uniqueness and advantages for wearable power supply as compared with rigid and liquid counterparts [3]. Particularly, the Pam-alginate double-network hydrogel provides excellent stretchability via two covalent crosslinks inclusive of the bond through N, N′-methylenebisacrylamide, and the bond between amine groups on Pam chains and carboxyl groups on alginate chains [46]. Thus, the Pam-alginate/EmimBF$_4$/PEG displays a remarkable tensile property that can be stretched to 20 times of its original length with an elastic modulus of 3.8 kPa (Fig. S22). Moreover, the excellent scalability and tailorable architecture of Pam-alginate/EmimBF$_4$/PEG enable the manufacture of devices in various sizes and shapes, featuring the device suitable for e-skin applications. We showcased a Pam-alginate/EmimBF$_4$/PEG wristband in Fig. 1A and Movie S1, and of which a ring-size sample was stretched several times larger and then fitted the wrist. The $V_{thermal}$ with a magnitude of 6.7 mV was generated at ~1 °C when the sample was attached to the skin (Fig. S23). Even though the theoretical ΔT could be as high as 8 °C (i.e., skin temperature of 32 °C − ambient temperature of 24 °C), the actual ΔT for the power output was estimated to be approximately 1 °C due to a large temperature drop at thermal contact and epidermis [47]. A Pam-alginate/EmimBF$_4$/PEG wristband was also demonstrated on a glass bottle (Fig. 5B), where the hot water and ice were added in turns. Fig. 5C depicts the real-time open-circuit voltage (V_{oc}) profile. The temperature of the outer wall of the glass bottle and the outer surface of the sample

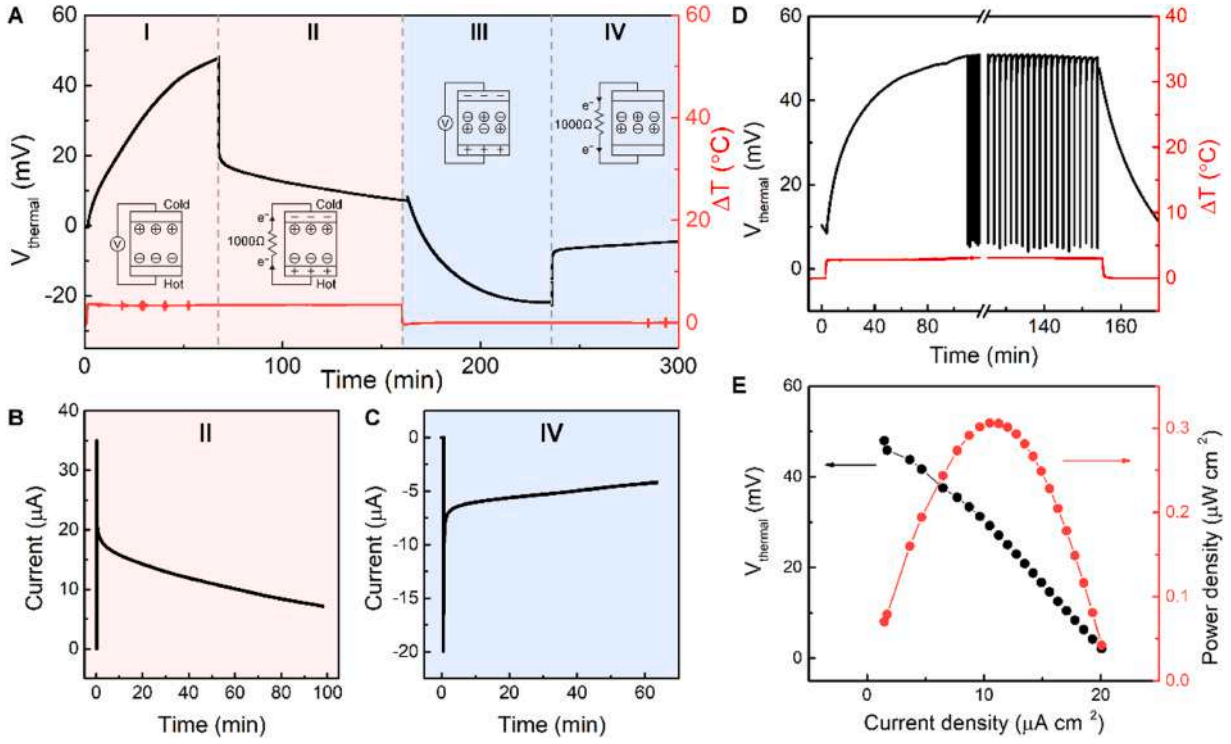

Fig. 4. Power generation in Pam-alginate/EmimBF$_4$/PEG. (A) Four-stage charging-discharging behaviors of Pam-alginate/EmimBF$_4$/PEG. Inserts present corresponding electron flow. (B) and (C) Current plots in electrical charging (stage II), and discharging (stage IV), respectively. (D) Thermovoltage profile in quasi-continuous charging/discharging process for 30 cycles. (E) Power density (red) and thermovoltage (black) of the first cycle in D.

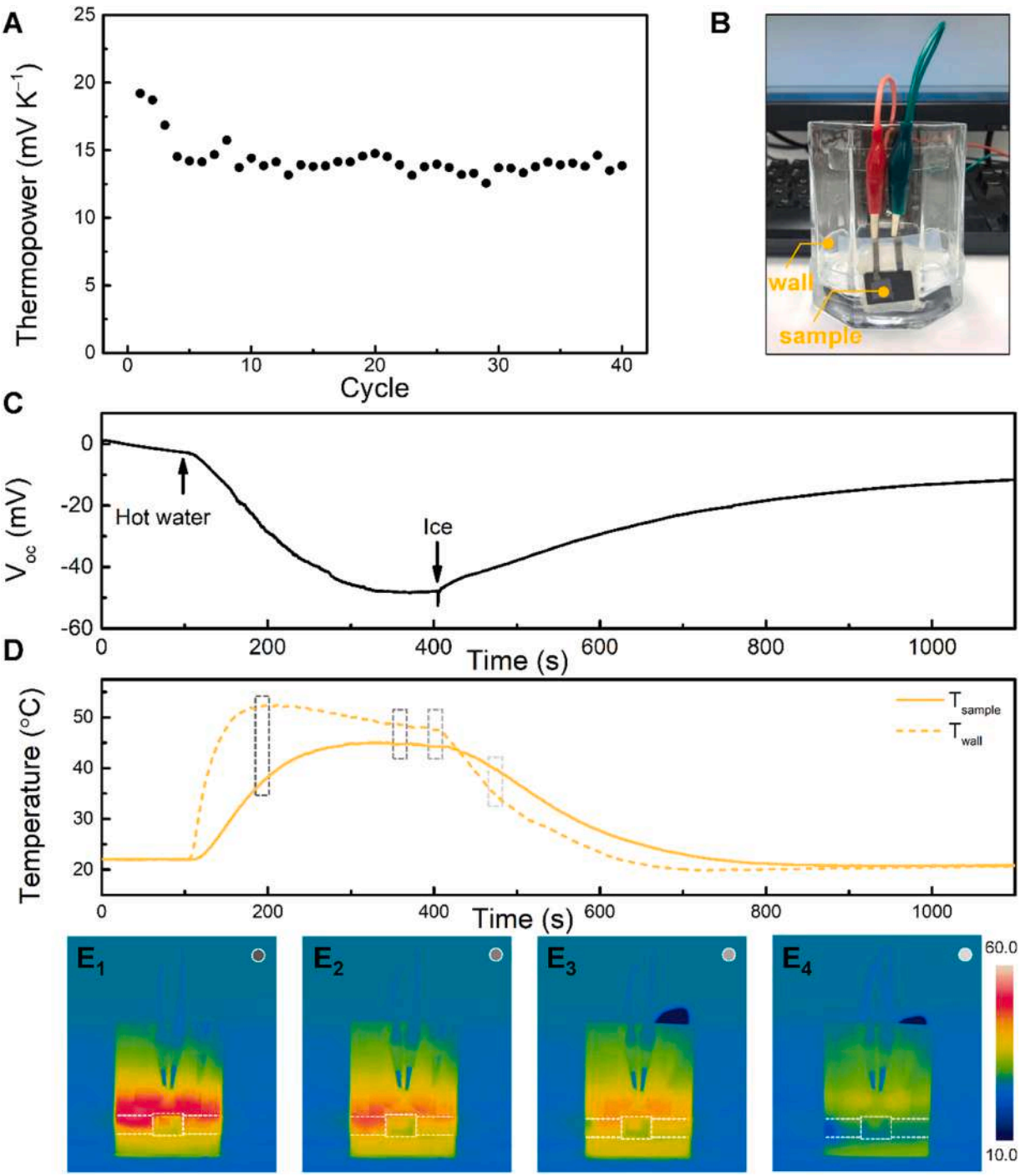

Fig. 5. Device cyclability and thermoelectric wristband demonstration. (A) Thermopower of Pam-alginate/EmimBF$_4$/PEG measured in each heating-cooling cycle. (B) Digital image of a Pam-alginate/EmimBF$_4$/PEG wristband bound to a glass bottle where the temperature at the wall of the bottle (T_{wall}) and the outside surface of the sample (T_{sample}) were recorded. (C) Open-circuit voltage (V_{oc}) and (D) Temperatures inclusive of T_{wall} and T_{sample} change with respect to time. (E_1-E_4) Infrared images captured at different times indicated with gray dashed box in D.

are denoted as T_{wall} and T_{sample}, respectively. When hot water was poured into the glass bottle, both T_{wall} and T_{sample} increased and T_{wall} increased much faster than T_{sample}, creating ΔT across the two CP electrodes (Fig. 5D). A V_{oc} change from −2.8 mV to −48.0 mV was observed at 400 s with a ΔT of 3.3 °C. After adding ice, T_{wall} and T_{sample} decreased along with reducing ΔT. The temperature and V_{oc} gradually returned while the ionic gradient slowly relaxed until the ΔT disappeared. The temperature profile of the glass bottle at four different times were captured by infrared imaging (Fig. 5E_1-E_4). This demonstration can be viewed in Movie S2.

3. Conclusions

In summary, an emerging i-TE consisting of the hydrogel electrolyte and CP electrodes is reported, which exhibits a S_i of 19.32 mV K^{-1} and power density of 0.31 μW cm^{-2}. Using 2D DOSY ^{1}H and ^{19}F NMR, we directly verified the mechanism of cation-localization and a giant disparity between cations and anions, that leads to the regulated ion transport. Additionally, the excellent moldability and stretchability of the Pam-alginate/EmimBF$_4$/PEG device show great promise for wearable power supply, as demonstrated by i-TE wristband with a large

$V_{thermal}$. Our work carries profound implications for the future development of i-TEs that beyond typical Seebeck effect, thermogalvanic effect, and Soret effect. Through further optimization, the proposed transpiration-driven mechanism not only can generate power but also may help heat dissipation, which is fundamentally not possible for typical i-TEs to accomplish at the same time. In this study, the incorporation of directional ion flux and selective ion-localization within versatile hydrogel is an effective strategy for giant thermoelectric signature, which holds the blueprint of new low-grade heat harvesters [12,28,48].

4. Methods

4.1. Materials

Acrylamide (≥99%, Sigma-Aldrich) monomer, N, N′-methylenebisacrylamide (BIS, 99%, Sigma-Aldrich) cross-linker, ammonium persulfate (APS, ≥98%, Sigma-Aldrich) initiator, sodium alginate (Sigma-Aldrich), 1-ethyl-3-methylimidazolium tetrafluoroborate ($EmimBF_4$, ≥99%, Sigma-Aldrich), and polyethylene glycol (M_w = 6000 Da, Sigma-Aldrich) were used without further purification. Deionized water (18.2 MΩ) was used throughout the experiments.

4.2. Preparation of ionic thermoelectric hydrogel

12.2 g acrylamide and 1.22 g alginate were dissolved in deionized water at 25 °C to make a 100 ml homogeneous aqueous solution. 2.19×10^{-5} mol APS initiator and 4.67×10^{-5} mol BIS cross-linker were added. The solution was degassed for 5 min in a vacuum chamber before being poured into a rectangular glass mold or a 3D-printing circular mold which were coated with a layer of releasing agent (Ease Release 200, Smooth-On). The molds were covered tightly by glass sheets to avoid contact with air. The Pam-alginate double-network hydrogel was cured under ultraviolet illumination for 1.5 h and then soaked in $EmimBF_4$ aqueous solutions with various concentrations (e.g., 1 M, 1.3 M, 1.5 M and 2 M) for 16 h. Then, Pam-alginate/$EmimBF_4$ was subjected to the second soaking step in 0.05 g ml^{-1} PEG aqueous solution for 1–3 h. The Pam-alginate/$EmimBF_4$/PEG samples were prepared by PEG with the molecular weight (M_w) of 6000 unless otherwise stated. The S_i as a function of PEG M_w and the effect of one-step soaking using a mixture of $EmimBF_4$ and PEG aqueous solution are discussed in Supplementary Note 4 (Figs. S24, S25).

4.3. Device fabrication

The liquid on the surface of the Pam-alginate/$EmimBF_4$/PEG hydrogel electrolyte was dried using the N_2 stream. The hydrogel electrolyte was sandwiched by nanoporous carbon papers (resistance 1.89 mΩ cm^{-2}), on which titanium foils were connected for collecting current due to their corrosion resistance and stability at our working temperature range. The thickness of the device is basically determined by the thickness of Pam-alginate/$EmimBF_4$/PEG hydrogel (2–3 mm). To prevent the water loss of hydrogels, polyolefin shrink films were utilized to encapsulate the entire device. Exceptionally, the wristband samples were sealed by polyolefin film partially for better fitting with our wrists and the glass bottle.

4.4. Electrochemical measurement

Electrochemical tests were performed using CHI 660E potentiostat. The heating and cooling were carried out on bottom and top electrodes by employing two thermoelectric modules, where the temperature was precisely controlled using the Labview program [29]. Besides, two thermocouples were placed upon and underneath the sample to record the temperatures at both sides, and the temperature measurement uncertainty was estimated to be ±0.5 °C.

EIS characterization was conducted using Gamry Reference 3000 potentiostat, and the samples were tested under open circuit condition with a voltage amplitude of 5 mV in the frequency range of 10–10^6 Hz. The ionic conductivity at different temperatures is calculated from $\sigma = \frac{L}{RA}$, where R is retrieved at the frequency when the phase angle is closest to 0, L is the distance between two carbon electrodes and A is the area of the electrodes.

4.5. Characterization

Liquid phase 1D and 2D-diffusion-ordered spectroscopy (DOSY) ^1H and ^{19}F nuclear magnetic resonance (NMR) experiments were performed on a 9.4 Tesla Bruker Advance III 400 MHz NMR spectrometer equipped with a 5 mm $^1H/^{19}F$ BBFO SmartProbe, and a Diff30 probehead with a selective RF-inset was used. 20 mg ml^{-1} $EmimBF_4$ aqueous solution and $EmimBF_4$ aqueous solutions with PEG at various concentrations (i.e., 10 mg ml^{-1}, 20 mg ml^{-1} and 40 mg ml^{-1}) were prepared in 0.5 ml D_2O. Stimulated echo bipolar gradient pulses with 2 spoil gradients were run in pseudo 2D mode with 32 increments for 2D-DOSY ^1H and ^{19}F NMR, operating at 400.1 and 376.45 MHz for ^1H and ^{19}F, respectively [49].

The in-situ heating DOSY ^1H and ^{19}F NMR experiments were carried out at three different temperatures (i.e., 21 °C, 30 °C and 40 °C) using a digital variable temperature unit (B-VT 3000).

^1H DOSY NMR for hydrogel was conducted on a Bruker Avance III 500 spectrometer equipped with a 4 mm ^1H resonance (HR) magic-angle spinning (MAS) probe head operating at 500 MHz ^1H Larmor frequency. The Pam-alginate hydrogel samples were prepared directly in the NMR tubes and of which the water is the mixture of H_2O/D_2O (9:1, v/v). The temperature was controlled at 21 °C for 15 min before the measurement.

The diffusion coefficient (D) is characterized based on the Stejskal-Tanner equation [35],

$$\ln\left(\frac{I_G}{I_0}\right) = -\gamma^2 G^2 \delta^2 \left(\Delta - \delta \Big/ 3\right) D = -ZD \tag{1}$$

$$Z = \gamma^2 G^2 \delta^2 (\Delta - \delta/3) \tag{2}$$

where G is the pulse-field gradient strength, Δ is the time separation between pulsed-gradients, δ is the duration of the pulses and γ is the gyromagnetic ratio. The I_G and I_0 are the signal intensity at G and G= 0, respectively, and the product $\gamma^2 G^2 \delta^2 (\Delta - \delta/3)$ is termed the Z value. All specific parameters adopted to DOSY ^1H and ^{19}F NMR measurements are discussed in Supplementary Note 3.

Raman spectra were obtained in the range of 200–4000 cm^{-1} using a confocal Raman microscope (LabRAM HR Evolution, Horiba) equipped with a diode-pump solid-state (DSPP) laser (532 nm) and a neutral-density filter (ND filter). The laser was focused using a 50× objective (NA = 0.5). The number of gratings in the Raman microscope was 600 groove mm^{-1}. The acquisition time of a single Raman spectrum was 8 s.

Thermal conductivity of Pam-alginate hydrogel with $EmimBF_4$ and PEG was measured using transient hot-wire method (TC3000 thermal conductivity meter, XIATech). Before each measurement, the temperature was kept for 20 min, and the measurement at each temperature was made in triplicate.

Mechanical tests of the hydrogels were conducted in air, at room temperature, using an Instron 3340 single column universal materials test machine equipped with pneumatic clamping. The loading rate was kept at 15 mm min^{-1}.

Differential scanning calorimetry (DSC) analysis was performed on Discovery DSC (TA Instruments) at the temperature range of 20–90 °C with a heating/cooling rate of 10 °C min^{-1} under nitrogen flow.

Appendix

Fig. 2C shows the thermopower of best reported TECs and i-TEs relying on various working principles from top to bottom: thermogalvanic effect: ferric/ferrous ($Fe^{2+/3+}$) aqueous electrolyte through graphene oxide/platinum (GO/Pt) cathode and PANI anode (GO/Pt | $Fe^{2+/3+}$ | PANI) [29]; ferri/ferrocyanide ($Fe(CN)_6^{3-/4-}$) aqueous electrolyte with guanidinium chloride (GdmCl) and urea through two graphite electrodes (Graphite | $Fe(CN)_6^{3-/4-}$-urea/GdmCl | Graphite) [23]; $Fe(CN)_6^{3-/4-}$ aqueous electrolyte with methanol through two platinum (Pt) electrodes (Pt | $Fe(CN)_6^{3-/4-}$-methanol | Pt) [22]; poly (vinylidene fluoride)/cobalt bipyridyl bis(trifluoromethanesulfonyl) amide with 3–methoxypropionitrile ($[Co(bpy)_3^{2+/3+}][NTf_2]_{2/3}$-MPN) in poly(vinylidene fluoride-cohexafluoropropylene) (PVDF-HPF) gel through Pt-Pt electrodes (Pt | $[Co(bpy)_3^{2+/3+}][NTf_2]_{2/3}$-MPN/PVDF -HFP | Pt) [25]; $Fe(CN)_6^{3-/4-}$ with cellulose matrix through two nickel (Ni) electrodes (Ni | $Fe(CN)_6^{3-/4-}$-cellulose | Ni);[21] $Fe(CN)_6^{3-/4-}$ in polyvinyl alcohol (PVA) gel through two gold/chromium (Au/Cr) electrodes (Au/Cr | $Fe(CN)_6^{3-/4-}$-PVA | Au/Cr) [2]; $Fe(CN)_6^{3-/4-}$ in sodium polyacrylate gel through Pt-Pt electrodes (Pt | $Fe(CN)_6^{3-/4-}$-sodium polyacrylate | Pt) [8]; $Fe^{2+/3+}$ in PVA gel through two Au/Cr electrodes (Au/Cr | $Fe^{2+/3+}$-PVA | Au/Cr).[2] Our work: Pam-alginate/$EmimBF_4$; Pam-alginate/$EmimBF_4$/PEG. Soret effect: 1-ethyl-3-methylimidazolium bis(trifluoromethylsulfony)imide (EmimTFSI) in PVDF-HFP gel through two gold (Au) electrodes (Au | EmimTFSI/PVDF-HFP | Au) [27]; poly(4-styrenesulfonic acid) (PSSH) polymer PSSH through two PANI coated electrodes containing graphite and CNT (PANI/CNT-G | PSSH | PANI/CNT-G) [26]; EmimTFSI with PEG in PVDF-HFP gel through Au-Au electrodes (Au | EmimTFSI-PEG/PVDF-HFP | Au) [27]; poly(3,4-ethylenedioxythiophene)-poly(styrenesulphonate) (PEDOT:PSS) polymer doped with PSSH through Au-Au electrodes (Au | PEDOT:PSS/PSSH | Au) [12]; $Fe(CN)_6^{3-/4-}$ with potassium chloride (KCl) in gelatin gel through two copper/gold (Cu/Au) electrodes (Cu/Au | $Fe(CN)_6^{3-/4-}$ /KCl | Cu/Au) [13]; PEDOT:PSS containing copper chloride ($CuCl_2$) through Au-Au electrodes (Au | PEDOT:PSS/$CuCl_2$ | Au) [14]; tetrabutyl ammonium nitrate (TBAN)-dodecanol organic electrolyte through Pt-Pt electrodes (Pt | TBAN-Dodecanol | Pt) [24]; polyethylene oxide (PEO)-NaOH aqueous electrolyte through two gold/carbon nanotubes (Au/CNT) electrodes (Au/CNT | PEO-NaOH | Au/CNT) [28]; PEO-NaOH aqueous electrolyte with cellulose membrane through Pt-Pt electrodes (Pt | PEO-NaOH-Cellulose | Pt) [15].

CRediT authorship contribution statement

C.L., Q.K.L. and S.P.F. conceived the concept and designed the experiments. C.L., Q.K.L. and S.J.W. conducted the experiments. N.X.F. contributed to the experiment design and thermopower analysis. W.S.L. contributed to NMR characterization. C.L., Q.K.L., S.P.F. and N.X.F. prepared the manuscript and contributed to the interpretation of the results. C.L. and Q.K.L. contribute equally to this work.

Declaration of Competing Interest

C.L., Q.K.L., and S.P.F. are inventors on a patent of US Appl. 63/017066, 2020. The authors declare no competing interests.

Acknowledgements

The authors would like to thank Y.Z.W. for sharing NMR HR MAS facility, and X. W., Z.W.Z. and Z.Y.W. for constructive discussion. This work was supported by the General Research Fund of the Research Grants Council of Hong Kong Special Administrative Region, China (Award No. 17206519 and 17206518), and the joint research center between MIT Mechanical Engineering and SUSTech.

Appendix A. Supporting information

Supplementary data associated with this article can be found in the online version at doi:10.1016/j.nanoen.2021.106738.

References

[1] S. Chu, A. Majumdar, Opportunities and challenges for a sustainable energy future, Nature 488 (2012) 294–303.
[2] P. Yang, K. Liu, Q. Chen, X. Mo, Y. Zhou, S. Li, G. Feng, J. Zhou, Wearable thermocells based on gel electrolytes for the utilization of body heat, Angew. Chem. Int. Ed. 55 (2016) 12050–12053.
[3] A.R.M. Siddique, S. Mahmud, B. Van Heyst, A review of the state of the science on wearable thermoelectric power generators (TEGs) and their existing challenges, Renew. Sustain. Energy Rev. 73 (2017) 730–744.
[4] J. Wu, J.J. Black, L. Aldous, Thermoelectrochemistry using conventional and novel gelled electrolytes in heat-to-current thermocells, Electrochim. Acta 225 (2017) 482–492.
[5] A. Zevalkink, D.M. Smiadak, J.L. Blackburn, A.J. Ferguson, M.L. Chabinyc, O. Delaire, J. Wang, K. Kovnir, J. Martin, L.T. Schelhas, T.D. Sparks, S.D. Kang, M. T. Dylla, G.J. Snyder, B.R. Ortiz, E.S. Toberer, A practical field guide to thermoelectrics: fundamentals, synthesis, and characterization, Appl. Phys. Rev. 5 (2018) 50.
[6] S.D. Kang, G.J. Snyder, Transport property analysis method for thermoelectric materials: material quality factor and the effective mass model, arXiv Preprint arXiv 1710 (2017) 06896.
[7] S.I. Kim, K.H. Lee, H.A. Mun, H.S. Kim, S.W. Hwang, J.W. Roh, D.J. Yang, W. H. Shin, X.S. Li, Y.H. Lee, Dense dislocation arrays embedded in grain boundaries for high-performance bulk thermoelectrics, Science 348 (2015) 109–114.
[8] G.H. Kim, L. Shao, K. Zhang, K.P. Pipe, Engineered doping of organic semiconductors for enhanced thermoelectric efficiency, Nat. Mater. 12 (2013) 719.
[9] B. Poudel, Q. Hao, Y. Ma, Y. Lan, A. Minnich, B. Yu, X. Yan, D. Wang, A. Muto, D. Vashaee, High-thermoelectric performance of nanostructured bismuth antimony telluride bulk alloys, Science 320 (2008) 634–638.
[10] T. Quickenden, Y. Mua, A review of power generation in aqueous thermogalvanic cells, J. Electrochem. Soc. 142 (1995) 3985–3994.
[11] S.W. Lee, Y. Yang, H.-W. Lee, H. Ghasemi, D. Kraemer, G. Chen, Y. Cui, An electrochemical system for efficiently harvesting low-grade heat energy, Nat. Commun. 5 (2014) 3942.
[12] T. Li, X. Zhang, S.D. Lacey, R. Mi, X. Zhao, F. Jiang, J. Song, Z. Liu, G. Chen, J. Dai, Cellulose ionic conductors with high differential thermal voltage for low-grade heat harvesting, Nat. Mater. 18 (2019) 608.
[13] B. Kim, J. Na, H. Lim, Y. Kim, J. Kim, E. Kim, Robust high thermoelectric harvesting under a self-humidifying bilayer of metal organic framework and hydrogel layer, Adv. Funct. Mater. 29 (2019), 1807549.
[14] C.-G. Han, X. Qian, Q. Li, B. Deng, Y. Zhu, Z. Han, W. Zhang, W. Wang, S.-P. Feng, G. Chen, Giant thermopower of ionic gelatin near room temperature, Science 368 (2020) 1091–1098.
[15] B. Kim, J.U. Hwang, E. Kim, Chloride transport in conductive polymer films for an n-type thermoelectric platform, Energy Environ. Sci. 13 (2020) 859–867.
[16] Y. Guo, J. Bae, F. Zhao, G. Yu, Functional hydrogels for next-generation batteries and supercapacitors, Trends Chem. 1 (2019) 335–348.
[17] M. Dietzel, S. Hardt, Thermoelectricity in confined liquid electrolytes, Phys. Rev. Lett. 116 (2016), 225901.
[18] K. Liu, T. Ding, J. Li, Q. Chen, G. Xue, P. Yang, M. Xu, Z.L. Wang, J. Zhou, Thermal–electric nanogenerator based on the electrokinetic effect in porous carbon film, Adv. Energy Mater. 8 (2018), 1702481.
[19] B.M. Savoie, M.A. Webb, T.F. Miller III, Enhancing cation diffusion and suppressing anion diffusion via Lewis-acidic polymer electrolytes, J. Phys. Chem. Lett. 8 (2017) 641–646.
[20] H.-N. Lee, N. Newell, Z. Bai, T.P. Lodge, Unusual lower critical solution temperature phase behavior of poly (ethylene oxide) in ionic liquids, Macromolecules 45 (2012) 3627–3633.
[21] L. Jin, G.W. Greene, D.R. MacFarlane, J.M. Pringle, Redox-active quasi-solid-state electrolytes for thermal energy harvesting, ACS Energy Lett. 1 (2016) 654–658.
[22] T. Kim, J.S. Lee, G. Lee, H. Yoon, J. Yoon, T.J. Kang, Y.H. Kim, High thermopower of ferri/ferrocyanide redox couple in organic-water solutions, Nano Energy 31 (2017) 160–167.
[23] J. Duan, G. Feng, B. Yu, J. Li, M. Chen, P. Yang, J. Feng, K. Liu, J. Zhou, Aqueous thermogalvanic cells with a high Seebeck coefficient for low-grade heat harvest, Nat. Commun. 9 (2018) 5146.
[24] M. Bonetti, S. Nakamae, M. Roger, P. Guenoun, Huge seebeck coefficients in nonaqueous electrolytes, J. Chem. Phys. 134 (2011), 114513.
[25] A. Taheri, D.R. MacFarlane, C. Pozo-Gonzalo, J.M. Pringle, Quasi-solid-state electrolytes for low-grade thermal energy harvesting using a cobalt redox couple, ChemSusChem 11 (2018) 2788–2796.
[26] S. Kee, N. Kim, B.S. Kim, S. Park, Y.H. Jang, S.H. Lee, J. Kim, J. Kim, S. Kwon, K. Lee, Controlling molecular ordering in aqueous conducting polymers using ionic liquids, Adv. Mater. 28 (2016) 8625–8631.
[27] D. Zhao, A. Martinelli, A. Willfahrt, T. Fischer, D. Bernin, Z.U. Khan, M. Shahi, J. Brill, M.P. Jonsson, S. Fabiano, Polymer gels with tunable ionic Seebeck coefficient for ultra-sensitive printed thermopiles, Nat. Commun. 10 (2019) 1093.

[28] D. Zhao, H. Wang, Z.U. Khan, J. Chen, R. Gabrielsson, M.P. Jonsson, M. Berggren, X. Crispin, Ionic thermoelectric supercapacitors, Energy Environ. Sci. 9 (2016) 1450–1457.
[29] X. Wang, Y.-T. Huang, C. Liu, K. Mu, K.H. Li, S. Wang, Y. Yang, L. Wang, C.-H. Su, S.-P. Feng, Direct thermal charging cell for converting low-grade heat to electricity, Nat. Commun. 10 (2019) 1–8.
[30] Y.-Z. Zheng, Y. Zhou, G. Deng, R. Guo, D.-F. Chen, A combination of FTIR and DFT to study the microscopic structure and hydrogen-bonding interaction properties of the [BMIM][BF4] and water, Spectrochim. Acta A. Mol. Biomol. Spectrosc. 226 (2020), 117624.
[31] B.R. Brown, Sensing temperature without ion channels, Nature 421 (2003), 495-495.
[32] B.R. Brown, M.E. Hughes, C. Russo, Thermoelectricity in natural and synthetic hydrogels, Phys. Rev. E 70 (2004), 031917.
[33] K. Saihara, Y. Yoshimura, S. Ohta, A. Shimizu, Properties of water confined in ionic liquids, Sci. Rep. 5 (2015) 10619.
[34] K. Hayamizu, Y. Aihara, H. Nakagawa, T. Nukuda, W.S. Price, Ionic conduction and ion diffusion in binary room-temperature ionic liquids composed of [emim][BF4] and LiBF4, J. Phys. Chem. B 108 (2004) 19527–19532.
[35] Y. Cohen, L. Avram, L. Frish, Diffusion NMR spectroscopy in supramolecular and combinatorial chemistry: an old parameter—new insights, Angew. Chem. Int. Ed. 44 (2005) 520–554.
[36] N.E. Heimer, R.E. Del Sesto, Z. Meng, J.S. Wilkes, W.R. Carper, Vibrational spectra of imidazolium tetrafluoroborate ionic liquids, J. Mol. Liq. 124 (2006) 84–95.
[37] V. Amoli, J.S. Kim, E. Jee, Y.S. Chung, S.Y. Kim, J. Koo, H. Choi, Y. Kim, D.H. Kim, A bioinspired hydrogen bond-triggered ultrasensitive ionic mechanoreceptor skin, Nat. Commun. 10 (2019) 1–13.
[38] T. Yamada, M. Mizuno, Characteristic spectroscopic features because of cation–anion interactions observed in the 700–950 cm–1 range of infrared spectroscopy for various imidazolium-based ionic liquids, ACS Omega 3 (2018) 8027–8035.
[39] Z. Xiao, R.G. Larson, Y. Chen, C. Zhou, Y. Niu, G. Li, Unusual phase separation and rheological behavior of poly (ethylene oxide)/ionic liquid mixtures with specific interactions, Soft Matter 12 (2016) 7613–7623.
[40] H. Cheng, X. He, Z. Fan, J. Ouyang, Flexible quasi-solid state ionogels with remarkable seebeck coefficient and high thermoelectric properties, Adv. Energy Mater. 9 (2019), 1901085.
[41] J.A. Widegren, E.M. Saurer, K.N. Marsh, J.W. Magee, Electrolytic conductivity of four imidazolium-based room-temperature ionic liquids and the effect of a water impurity, J. Chem. Thermodyn. 37 (2005) 569–575.
[42] Y. Yusof, M. Shukur, M. Hamsan, K. Jumbri, M.F.Z. Kadir, Plasticized solid polymer electrolyte based on natural polymer blend incorporated with lithium perchlorate for electrical double-layer capacitor fabrication, Ionics 25 (2019) 5473–5484.
[43] X. Xie, D. Li, T.-H. Tsai, J. Liu, P.V. Braun, D.G. Cahill, Thermal conductivity, heat capacity, and elastic constants of water-soluble polymers and polymer blends, Macromolecules 49 (2016) 972–978.
[44] N. Kim, S. Lienemann, I. Petsagkourakis, D.A. Mengistie, S. Kee, T. Ederth, V. Gueskine, P. Leclere, R. Lazzaroni, X. Crispin, K. Tybrandt, Elastic conducting polymer composites in thermoelectric modules, Nat. Commun. 11 (2020) 10.
[45] Z.A. Akbar, J.W. Jeon, S.Y. Jang, Intrinsically self-healable, stretchable thermoelectric materials with a large ionic Seebeck effect, Energy Environ. Sci. 13 (2020) 2915–2923.
[46] J.-Y. Sun, X. Zhao, W.R. Illeperuma, O. Chaudhuri, K.H. Oh, D.J. Mooney, J. J. Vlassak, Z. Suo, Highly stretchable and tough hydrogels, Nature 489 (2012) 133.
[47] H. Park, Y. Eom, D. Lee, J. Kim, H. Kim, G. Park, W. Kim, High power output based on watch-strap-shaped body heat harvester using bulk thermoelectric materials, Energy 187 (2019), 115935.
[48] A.D. Poletayev, I.S. McKay, W.C. Chueh, A. Majumdar, Continuous electrochemical heat engines, Energy Environ. Sci. 11 (2018) 2964–2971.
[49] G. Dal Poggetto, D.C. Favaro, M. Nilsson, G.A. Morris, C.F. Tormena, 19F DOSY NMR analysis for spin systems with nJFF couplings, Magn. Reson. Chem. 52 (2014) 172–177.